ADVANCED FUNCTIONAL MATERIALS
www.afm-journal.de

Harnessing Interfacial Cl^- Ions for Concurrent Formate Production at Industrial Level via CO_2 Reduction and Methanol Oxidation

Yiqun Chen, Yan Zhang, Zhen Li, Biao Feng, Mengting Li, Qiang Wu, Zheng Hu, and Lawrence Yoon Suk Lee**

The efficient electrocatalytic conversion of CO_2 to formate is often impeded by the high energy requirements of the oxygen evolution reaction (OER) and the limited activity and selectivity of CO_2 reduction reaction (CO_2RR). Herein, a novel strategy to enhance formate production by substituting the OER with the methanol oxidation reaction (MOR) and optimizing the cathodic microenvironment with interfacial Cl^- ions is presented. Through theoretical analysis, binder-free Bi and NiOOH electrodes that achieve remarkable Faradaic efficiencies ($FE_{formate}$) exceeding 90% at current densities of 50–250 mA·cm^{-2} for CO_2RR and MOR, respectively, are identified. These combined experimental and theoretical investigations demonstrate that interfacial Cl^- enrichment on the Bi electrode modulates the local electronic structure, fostering a microenvironment conducive to CO_2RR. The Bi–NiOOH full cell maintains a $FE_{formate}$ above 90% at industry-level current densities (100–300 mA·cm^{-2}), enabling concurrent formate electrosynthesis at both electrodes. This work highlights the critical role of local anion environments in electrocatalysis and provides a strategic framework for the synergistic engineering of electrochemical systems.

1. Introduction

The global economy's reliance on fossil fuels has resulted in excessive CO_2 emissions and consequent climate issues.[1] To promote sustainable development, various carbon management strategies have been proposed, including carbon capture, storage, and utilization.[2] Among these, the electrochemical reduction of CO_2 powered by renewable electricity stands out as a promising approach due to its mild operating conditions, net-zero pollution, and potential to generate value-added products.[3] Formate, a product derived from the CO_2 reduction reaction (CO_2RR), has gained considerable attention for its potential as a hydrogen carrier for fuel cells and a key raw material for chemical feedstock.[4] In this context, *p*-block metals such as Sn,[5] In,[6] and Bi[7] are attractive cathodic catalysts due to their unique oxygenophilic properties.[8] For large-scale deployment of CO_2 reduction to formate ($CO_2RR_{formate}$), it is essential to develop robust electrochemical systems that meet the stringent techno-economic performance targets. These include achieving high Faradaic efficiencies of formate production ($FE_{formate} > 90\%$) and industry-level current densities ($J > 100$ mA·cm^{-2}).[9]

Traditional electrocatalytic systems for CO_2RR typically consist of an anode for the oxygen evolution reaction (OER) and a cathode for CO_2RR, separated by a membrane. While much research has focused on designing efficient electrocatalysts or devices for CO_2RR, the anodic component often receives less attention.[10] To achieve a synergistic "1 + 1 > 2" effect for industrial-scale production, both sides of the system must be engineered collaboratively.[11] The OER at the anode is energy-intensive and kinetically sluggish due to its complex four-electron pathway reaction, and it produces low-value O_2.[12] Therefore, replacing OER with a more thermodynamically favorable reaction that yields value-added chemicals is essential. By substituting OER with a suitable organic transformation reaction, the applied potential can be lowered, saving energy consumption and generating valuable products, effectively turning "waste" into "treasure" at the anode.[13] Ideally, the anodic organic transformation should work in tandem with the cathodic CO_2RR to simultaneously produce formate, doubling the production rate and

Y. Chen, Z. Li, M. Li, L. Y. S. Lee
Department of Applied Biology and Chemical Technology and Research Institute for Smart Energy
The Hong Kong Polytechnic University
Hung Hom, Kowloon, Hong Kong SAR, China
E-mail: lawrence.ys.lee@polyu.edu.hk
Y. Zhang, B. Feng, Q. Wu, Z. Hu
Key Laboratory of Mesoscopic Chemistry of MOE and Jiangsu Provincial Lab for Nanotechnology
School of Chemistry and Chemical Engineering
Nanjing University
Nanjing 210023, China
E-mail: wqchem@nju.edu.cn
L. Y. S. Lee
Department of Chemical Engineering (Integrated Engineering)
Kyung Hee University
1732 Deogyeong-daero, Giheung-gu, Yongin-si, Gyeonggi-do 17104, Republic of Korea

The ORCID identification number(s) for the author(s) of this article can be found under https://doi.org/10.1002/adfm.202505074

DOI: 10.1002/adfm.202505074

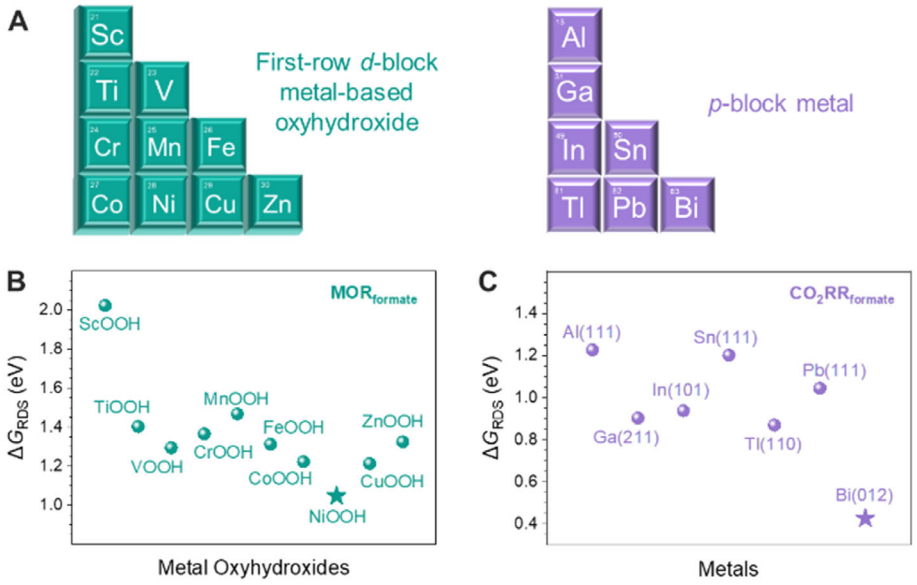

Figure 1. DFT optimization of active metal species. A) Database for DFT calculations. ΔG_{RDS} values of B) the first-row *d*-block metal-based oxyhydroxide for methanol-to-formate conversion and C) *p*-block metals for CO_2-to-formate conversion.

economic benefit. The methanol oxidation reaction (MOR) is a promising candidate due to methanol's low cost, high activity,[14] and its ability to produce semi-oxidized formate using transition metal-based catalysts[15] or fully-oxidized CO_2 using Pt-based catalysts.[16] For formate production, first-row *d*-block metal-based (oxy)hydroxides are promising catalysts due to their ability to alternate valence states between M^{2+} and M^{3+}, reconstructing active sites during the semi-oxidation process.[17]

To maximize catalytic activity, optimizing active metal species for both $CO_2RR_{formate}$ and MOR to formate ($MOR_{formate}$) is crucial. Density functional theory (DFT) serves as a powerful tool for identifying active phases with suitable descriptors.[18] Herein, through DFT optimization of *d*-block metal-based oxyhydroxide and *p*-block metals, NiOOH and Bi have been identified as the most active species for MOR and CO_2RR, respectively, for constructing electrocatalysts to concurrently produce formate. Binder-free NiOOH and Bi electrodes, synthesized via electrodeposition, exhibit high $FE_{formate}$ of over 90% at current densities of 50–250 $mA{\cdot}cm^{-2}$ for their respective reactions. When assembled into a Bi–NiOOH full cell, the system maintains a $FE_{formate}$ of over 90% at industry-level current densities of 100–300 $mA{\cdot}cm^{-2}$ for concurrent formate electrosynthesis. Notably, interfacial Cl^- enrichment on the Bi electrode, resulting from precursor reduction, creates a reaction-favoring microenvironment by regulating the local electronic structure, enhancing CO_2RR compared to Cl^--free electrode. This study demonstrates the importance of local anion microenvironment for electrocatalysis and provides valuable insights for synergistically engineering electrochemical systems.

2. Results and Discussion

2.1. DFT Optimization of Metal Species

Ideally, the anode and the cathode should be thermodynamically favorable for MOR and CO_2RR, respectively. Through DFT optimization, we identified preferential metal species, as depicted in **Figure 1**. Earth-abundant first-row *d*-block metal-based (oxy)hydroxides are promising for MOR catalysis due to their ability to alternate between M^{2+} and M^{3+} states, reconstructing active sites.[17] *P*-block metals are appealing for CO_2-to-formate conversion because of their unique oxygenophilic properties (Figure 1A).[8] The selection of crystal surfaces for model construction was guided by their thermodynamic stability, as determined by XRD analysis. The crystal plane with the highest signal intensity in XRD standard cards signifies the most favorable formation in metals, identifying it as the most thermodynamically stable surface. These surfaces are pivotal in electrocatalysis, hence our focus on them for model construction. Free energy changes (ΔG) at each elementary reaction step were calculated, with the ΔG of the rate-determining step (ΔG_{RDS}) used as a descriptor (Figure S1, Supporting Information). For MOR, the (001) plane of metal oxyhydroxides is the most stable, with NiOOH exhibiting the lowest ΔG_{RDS} of 1.05 eV (Figure 1B). For CO_2RR, the Bi(012) configuration, the thermodynamically most stable crystal surface of Bi, shows the lowest ΔG_{RDS} of 0.43 eV (Figure 1C). Based on these findings, NiOOH and Bi are selected as the anode and cathode materials, respectively.

2.2. Characterizations of h-$Ni(OH)_2$ and Its Anodic MOR Performance

Both the anode and cathode were synthesized via electrodeposition. The anode, composed of NiOOH derived from a hierarchical $Ni(OH)_2$ (h-$Ni(OH)_2$) precursor on nickel foam, was synthesized in a $Ni(NO_3)_2$ electrolyte. **Figure 2** summarizes the characterizations and performance of the anode. Scanning electron microscopic (SEM) image reveals a hierarchical structure of h-$Ni(OH)_2$ with uniformly distributed nanosheets (Figure 2A). X-ray diffraction (XRD) confirms the pure $Ni(OH)_2$ phase

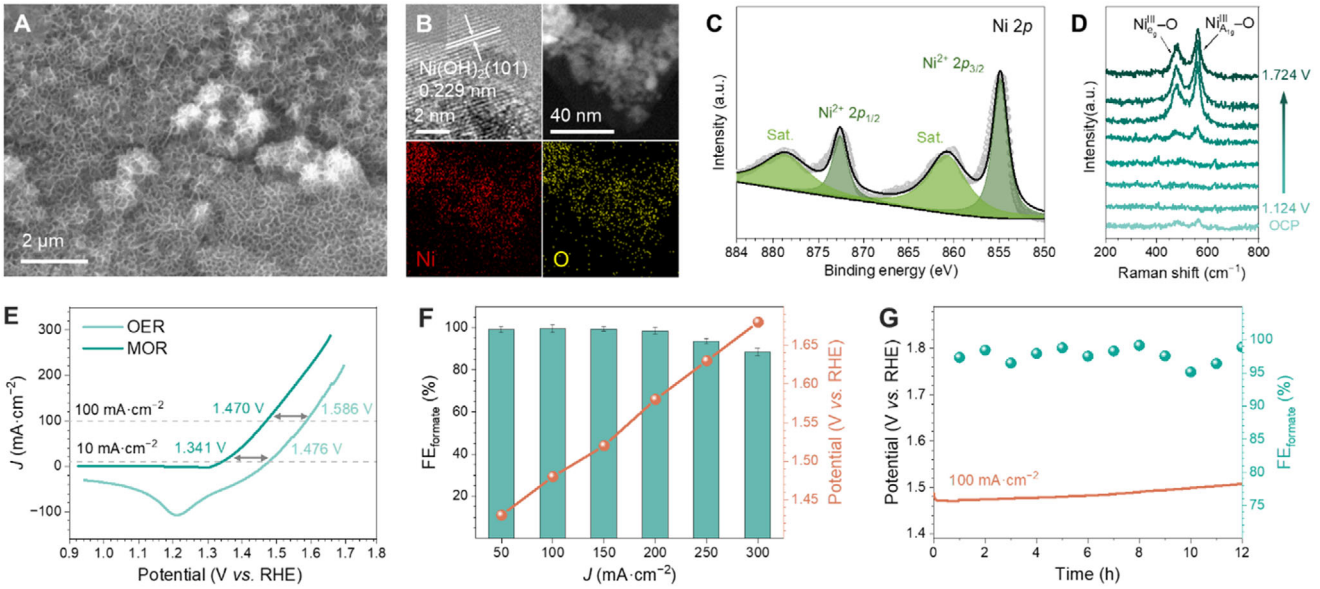

Figure 2. Characterizations and performance of h-Ni(OH)$_2$ anode. A) SEM, B) HRTEM and EDS mapping images, C) Ni 2*p* XPS spectrum, D) in situ Raman spectra, E) OER and MOR polarization curves, F) $FE_{formate}$ of MOR at various potentials and current densities, and G) MOR chronopotentiogram with $FE_{formate}$.

(Figure S2, Supporting Information), while energy-dispersive X-ray spectroscopic (EDS) mapping images disclose a uniform distribution of Ni and O elements, confirming the formation of h-Ni(OH)$_2$. A lattice fringe of 0.229 nm is evident from a high-resolution TEM (HRTEM) image, which corresponds to the (101) plane of Ni(OH)$_2$ (Figure 2B), consistent with XRD results. X-ray photoelectron spectrum (XPS) of h-Ni(OH)$_2$ in the Ni 2*p* region exhibits Ni^{2+} $2p_{1/2}$ and Ni^{2+} $2p_{3/2}$ peaks at 872.2 and 854.7 eV, respectively,[19] further confirming the main phase of Ni(OH)$_2$ in h-Ni(OH)$_2$ (Figure 2C). During MOR, the h-Ni(OH)$_2$ precursor undergoes electrooxidation to form the "real" active species NiOOH, as evidenced by in situ Raman spectra collected between open-circuit potential (OCP) and 1.724 V (vs reversible hydrogen electrode, RHE). Two peaks at 475 and 560 cm^{-1}, corresponding to the symmetric (NiIII eg–O) and anti-symmetric (NiIII A1g–O) stretching vibrations of O–Ni–O in NiOOH, respectively, emerge at ≈1.424 V and intensify as potential increases, indicating the in situ reconstruction of Ni(OH)$_2$ to NiOOH during MOR (Figure 2D).[20] Under a fixed potential, these two peaks rapidly emerge and maintain their intensity, confirming the stability of the NiOOH active species for MOR (Figure S3, Supporting Information). In contrast, the characteristic peaks for Ni foam appear at a more positive potential of 1.624 V, and their intensity is significantly weaker than that of h-Ni(OH)$_2$. This indicates the difficulty in conversion to NiOOH active species and the poor MOR performance of Ni foam (Figure S4, Supporting Information).

The anodic performance was evaluated in a three-electrode system. The optimized h-Ni(OH)$_2$, synthesized with an electrodeposition potential of −2.0 V versus Ag/AgCl and electrodeposition time of 15 min, requires overpotentials of 1.476 and 1.586 V to reach current densities of 10 and 100 mA·cm^{-2}, respectively, for OER in 1 M KOH (Figure S5, Supporting Information). Upon the addition of 1 M methanol, these overpotentials significantly decrease to 1.341 and 1.470 V, respectively, indicating a shift of anodic reaction from OER to MOR (Figure 2E). This reduction in overpotential is due to the faster MOR kinetics compared to OER, as reflected by the lower Tafel slope for MOR (23 mV·dec^{-1}) than OER (35 mV·dec^{-1}, Figure S6, Supporting Information). Product analysis using chronopotentiometry and ^{1}H nuclear magnetic resonance (NMR) spectroscopy confirms the exclusive formate production at current densities from 50 to 200 mA·cm^{-2}, with $FE_{formate}$ reaching nearly 100% at 1.43–1.58 V (Figure S7, Supporting Information). Even at current densities above 200 mA·cm^{-2}, $FE_{formate}$ remains high (>88%), indicating excellent selectivity and activity of h-Ni(OH)$_2$ (Figure 2F). The decrease of $FE_{formate}$ under high current density can be attributed to the inevitable enhancement of competing OER during MOR (Figure S8, Supporting Information). The h-Ni(OH)$_2$ also exhibits good stability, with a negligible potential decay (≈2%) and stable $FE_{formate}$ (>95%) during a continuous 12-h reaction at 100 mA·cm^{-2} (Figure 2G). The exceptional $MOR_{formate}$ performance of h-Ni(OH)$_2$ can be attributed to the *in-situ*-formed NiOOH species with a large electrochemical active surface area (ECSA) of 1.56 mF·cm^{-2} and a small charger transfer resistance (R_{ct}) of 0.31 Ω, as well as thermodynamically favorable reaction pathway and rapid reaction kinetics (Figure S9, Supporting Information). The h-Ni(OH)$_2$ outperforms most reported non-precious metal-based catalysts (Table S1, Supporting Information), demonstrating its potential to substitute OER with MOR to produce value-added products while reducing energy consumption.

2.3. Morphological and Structural Characterizations of h-Bi@Cl and h-Bi

Similar to h-Ni(OH)$_2$, the cathode was prepared using a two-step electrodeposition process. Initially, the hierarchical BiOCl

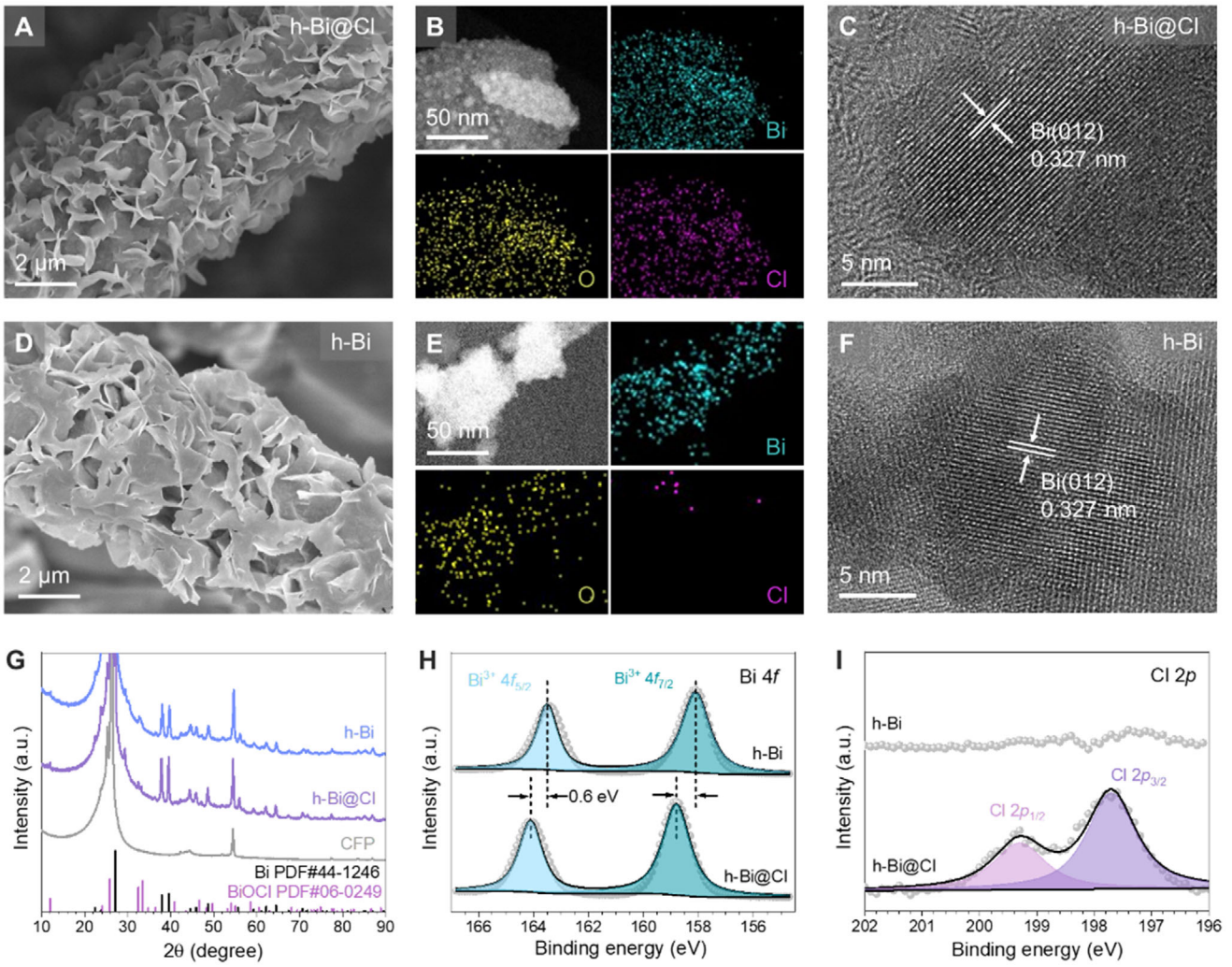

Figure 3. Morphological and structural characterizations of h-Bi@Cl and h-Bi. A) SEM, B) EDS mapping, and C) HRTEM images of h-Bi@Cl. D) SEM, E) EDS mapping, and F) HRTEM images of h-Bi. G) XRD patterns, H) Bi 4*f* XPS spectra, and I) Cl 2*p* XPS spectra of h-Bi@Cl and h-Bi.

(h-BiOCl) precursor on carbon fiber paper (CFP) was synthesized using a $Bi(NO_3)_3$/HCl electrolyte, with optimized synthetic conditions of electrodeposition at −1.0 V for 90 s (Figures S10 and S11, Supporting Information). The cathode, hierarchical Bi with Cl^- ions adsorbed on the surface (h-Bi@Cl), was obtained through a second electroreduction in 0.1 M $KHCO_3$. A control sample, hierarchical Bi without adsorbed Cl^- ions (h-Bi), was also synthesized by extending the electroreduction time and thoroughly washing the electrode. The SEM image in **Figure 3A** shows that h-Bi@Cl retains the unique hierarchical structure of h-BiOCl, featuring ordered nanosheets on CFP. EDS mapping images disclose a uniform distribution of Bi, O, and Cl elements, indicating Cl^- ion adsorption on the Bi surface (Figure 3B). The HRTEM image of h-Bi@Cl reveals a lattice fringe of 0.327 nm, corresponding to the (012) plane of Bi, which agrees well with DFT optimization results (Figure 3C). A similar morphology and crystal structure are observed in h-Bi, but Cl is absent from its EDS mapping image, confirming the successful removal of Cl^- ions (Figure 3D–F). The XRD patterns of both h-Bi@Cl and h-Bi display only the characteristic peaks of Bi at 27°, 28°, and 39.6°, confirming the complete reduction of BiOCl to Bi (Figure 3G).

While Cl^- ions have a negligible impact on the physical phase, they significantly influence the surface electronic distribution, as evidenced by Bi 4*f* XPS spectra. In the case of h-Bi, the inevitable oxidation of the surface Bi results in the absence of Bi^0 species, leading to Bi^{3+} $4f_{5/2}$ and $4f_{7/2}$ peaks at 163.5 and 158.1 eV, respectively.[21] In contrast, these peaks positively shift by 0.6 eV in h-Bi@Cl, indicating electron transfer from Bi to the electron-withdrawing Cl^- ions (Figure 3H). Additionally, two peaks at 199.3 and 197.7 eV in the Cl 2*p* XPS spectrum confirm the presence of interfacial Cl^- ions in h-Bi@Cl,[22] which are absent in h-Bi (Figure 3I). The presence of Cl^- ions is further validated by UV-Vis spectroscopy via turbidimetry, in agreement with Cl 2*p* XPS results (Figure S12, Supporting Information). Both h-Bi@Cl and h-Bi display comparable surface roughness and wettability, evidenced by contact angles of 30 ° for h-Bi@Cl and 26° for h-Bi (Figure S13, Supporting Information). Elemental analysis reveals similar Bi content (58.34 wt.% in h-Bi@Cl and 57.55 wt.% in h-Bi) but a marked difference in Cl content (5.02 at.% in h-Bi@Cl

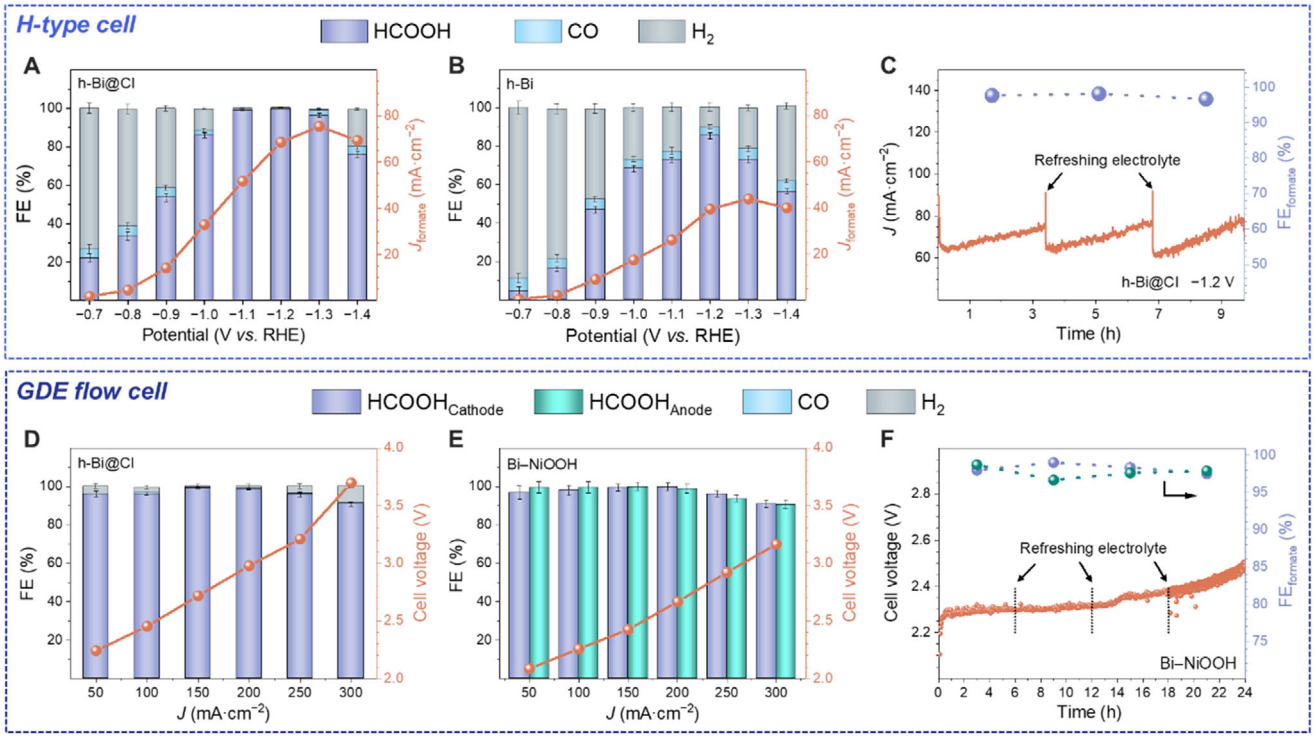

Figure 4. Cathodic CO_2RR and full cell performances. Cathodic CO_2RR performances of A) h-Bi@Cl and B) h-Bi. C) Chronoamperogram of h-Bi@Cl in an H-type cell. D) Cathodic CO_2RR performance of h-Bi@Cl. E) Full cell performance and F) chronoamperogram of h-Bi@Cl in a GDE flow cell.

and 1.04 at.% in h-Bi, Table S2, Supporting Information). These findings indicate that h-Bi@Cl and h-Bi share nearly identical morphology and structure, differing solely in the surface adsorption of Cl^- ions.

2.4. Cathodic CO_2RR and Full Cell Performance

The electrocatalytic CO_2RR performance of h-Bi@Cl and h-Bi was evaluated using two cell configurations: a customized H-type cell with two compartments separated by a Nafion117 proton exchange membrane (three-electrode system) and a gas diffusion electrode (GDE)-based flow cell separated by anion exchange membrane (two-electrode system, **Figure 4**). Cyclic voltammograms (CVs) and linear sweep voltammograms (LSVs) of both samples show significantly higher current responses in CO_2-saturated $KHCO_3$ compared to Ar-saturated $KHCO_3$, indicating their CO_2RR activity (Figure S14, Supporting Information). Notably, h-Bi@Cl exhibits a larger current response than h-Bi, suggesting superior CO_2RR activity. CO_2RR product analysis was conducted using chronoamperometry at various potentials for 30 min. Liquid products in the electrolyte were collected for NMR analysis, while gaseous products were analyzed by online gas chromatography. The only liquid product detected is formate, while the gaseous products are CO and H_2 (Figures S15 and S16, Supporting Information). In the H-type cell, h-Bi@Cl delivers a high $FE_{formate}$ plateau of over 95% across a wide potential window of −1.1 to −1.3 V, with a maximum value of 99.8% at −1.2 V and a maximum $J_{formate}$ of 75.5 mA·cm^{-2} at −1.3 V (Figure 4A). In contrast, h-Bi exhibits inferior performance, with a lower $FE_{formate}$ of only 85.5% at −1.2 V and a $J_{formate}$ of 43.8 mA·cm^{-2} (Figure 4B). Additionally, h-Bi@Cl maintains a current density of ≈70 mA·cm^{-2} and a $FE_{formate}$ above 95% during continuous electrocatalysis at −1.2 V for over 10 h (3 cycles), demonstrating excellent stability (Figure 4C). In situ Raman spectroscopy analysis of dynamic structural changes during CO_2RR reveals that both h-Bi@Cl and h-Bi maintain stable Bi–Bi species, while Bi–O species gradually diminish due to self-reduction (Figure S17, Supporting Information). To access its potential for large-scale applications, h-Bi@Cl was incorporated into a two-electrode GDE flow cell. The h-Bi@Cl maintains a $FE_{formate}$ of over 90% at current densities ranging from 50 to 300 mA·cm^{-2}, with a maximum $FE_{formate}$ of 99.0% at 150 mA·cm^{-2}. Correspondingly, the cell voltage increases from 2.2 to 3.7 V (Figure 4D). At these current densities, the formate crossover effect is negligible (Figure S18, Supporting Information).[23] The excellent CO_2RR performance of h-Bi@Cl, with its $FE_{formate}$ of >90% at industrial-level current densities, ranks it among the top-tier catalysts for $CO_2RR_{formate}$ (Table S3, Supporting Information).

Given the excellent performances of h-Ni$(OH)_2$ and h-Bi@Cl in MOR and CO_2RR, respectively, a promising strategy is to combine these two components into a single electrocatalytic system for concurrent formate production. We integrated h-Bi@Cl and h-Ni$(OH)_2$ into a GDE flow cell, serving as the anode and cathode, respectively, to form a Bi–NiOOH full cell. This Bi–NiOOH full cell achieves a high $FE_{formate}$ of over 90% at both cathode and anode across a current density range of 50–300 mA·cm^{-2}, demonstrating its potential for industrial-level formate production by effectively doubling the production rate (Figure 4E), which outperforms most recently reported cells (Table S4, Supporting

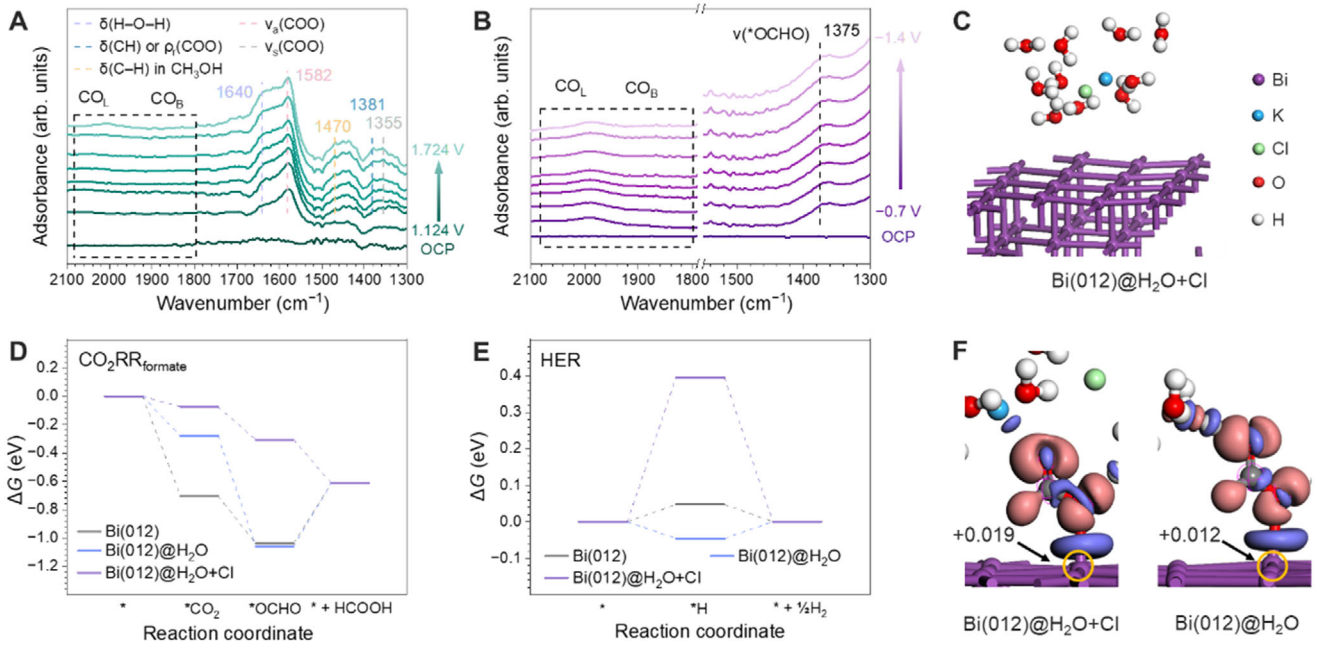

Figure 5. In situ characterizations and theoretical analysis of reaction mechanisms. In situ FTIR spectra of A) h-Ni(OH)$_2$ for MOR and B) h-Bi@Cl for CO_2RR. C) Model of Bi(012)@H_2O+Cl. ΔG values for D) $CO_2RR_{formate}$ and E) HER calculated for Bi(012), Bi(012)@H_2O, and Bi(012)@H_2O+Cl. F) Differential charge and population analyses of Bi(012)@H_2O+Cl and Bi(012)@H_2O.

Information). Notably, within this current density range, the corresponding cell voltage ranges from 2.3 to 3.2 V, resulting in a 40% reduction in electricity consumption compared to the conventional CO_2RR + OER system (2.2–3.7 V). Additionally, our techno-economic analysis reveals that MOR outperforms formaldehyde oxidation, due to its toxicity and higher cost relative to methanol and ethylene glycol oxidation, which is limited by glycolic acid co-production.[24] When powered by renewable energy, energy consumption and pollution release are effectively negligible. The Bi–NiOOH full cell offers substantial economic benefits for formate production at both electrodes, yielding a positive return (+44.98 HK$ mol^{-1} for CO_2RR and +7.35 HK$ mol^{-1} for MOR, based on purchase/sell prices in Hong Kong). This suggests substantial scalability potential by assembling multiple Bi–NiOOH full cells into stacks with ampere-level outlet (Table S5, Supporting Information). Our integration strategy offers several advantages: 1) Doubling the production rate; 2) Reducing electricity consumption; and 3) Generating valuable formate with a positive economic return. The Bi–NiOOH cell also exhibits excellent stability, maintaining a $FE_{formate}$ of over 95% and an unattenuated cell voltage of 87% during continuous operation for 24 h (4 cycles, Figure 4F). After the reaction, both the anode and cathode retain their hierarchical structures and active species, indicating their morphological and structural robustness (Figure S19, Supporting Information). Even under extended operation (100 h) at a high current density (200 mA cm^{-2}), the Bi–NiOOH full cell maintains excellent durability and structural stability (Figures S20A–C, Supporting Information). Despite the robustness of the catalysts, the cell voltage increases after prolonged continuous electrocatalysis. This performance deterioration can be attributed to a pH decrease resulting from the inevitable formation of carbonate/bicarbonate species due to CO_2 consumption, which elevates the device's internal resistance and, consequently, the cell voltage (Figure S20D, Supporting Information).[25]

2.5. Mechanistic Investigation

To elucidate the mechanism, a comprehensive investigation is necessary to identify reaction intermediates and analyze the impact of the reaction microenvironment from both experimental and theoretical perspectives. The in situ Fourier transform infrared (FTIR) spectra of h-Ni(OH)$_2$ for MOR and h-Bi@Cl for CO_2RR confirm the key intermediates (**Figure 5**). For MOR, the bands at 1582, 1381, and 1355 cm^{-1} are characteristic of formate, corresponding to the antisymmetric stretching vibration (ν_a(COO)), in-plane bending vibration (δ(CH)) or rocking mode (ρ_r(COO)), and symmetric stretching vibration of formate (vs (COO)), respectively (Figure 5A).[26] The band at 1640 cm^{-1} is attributed to water deformation (δ(H—O—H)), and the band at 1470 cm^{-1} corresponds to the in-plane bending vibration of C—H (δ(C—H)) in CH_3OH.[27] No bands for bridge-bonded CO (CO_B) or linearly-bonded CO (CO_L) were detected in the 1800–2100 cm^{-1} range, indicating the absence of CO_2 intermediates in the MOR process. Additionally, the absence of a CO_3^{2-} band ≈1400 cm^{-1} confirms that further oxidation beyond HCOOH formation is unfavorable. This analysis supports the MOR pathway on h-Ni(OH)$_2$ as $CH_3OH \rightarrow {}^*CH_3OH \rightarrow {}^*CH_3O \rightarrow {}^*CH_2O \rightarrow {}^*CHO \rightarrow {}^*HCOOH \rightarrow HCOOH$, consistent with the reaction pathway used in DFT optimization (Figure 1). For CO_2RR, a distinct signal at 1375 cm^{-1} for h-Bi@Cl is attributed to the vibration of the *OCHO intermediate (Figure 5B),[28] consistent with the in situ Raman results detecting *OCHO intermediates (Figures S17C,D, Supporting Information). In contrast, the CO_B and CO_L bands

in the 1800–2100 cm^{-1} range are significantly weaker, indicating a lower selectivity for CO compared to formate in CO_2RR.[22] This analysis suggests the CO_2RR pathway on h-Bi@Cl as CO_2 → $^*CO_2$ → $^*OCHO$ → $^*HCOOH$ → HCOOH, aligning with the DFT-optimized reaction pathway (Figure 1).

However, the reaction conditions for the h-Ni$(OH)_2$ anode and the h-Bi@Cl cathode differ significantly. The h-Ni$(OH)_2$ anode for MOR involves a straightforward solid–liquid two-phase reaction with a uniform reaction microenvironment and minimal changes. In contrast, the h-Bi@Cl cathode for CO_2RR involves a more complex solid–liquid–gas three-phase reaction, with a dynamic reaction microenvironment due to Cl^- ion release, which contributes to the performance differences between h-Bi@Cl and h-Bi (Figure 4). Gaining a deep understanding of the different interfacial conditions between h-Bi@Cl and h-Bi, specifically, the presence or absence of Cl^- ions, is essential as it leads to variations in the reaction microenvironment and the resulting catalytic activity. This can be comprehensively understood from both theoretical and experimental perspectives. From a theoretical viewpoint, as shown in Figure 5C–F, DFT calculations are employed to reveal the activity of Bi with or without Cl^- ions. The most thermodynamically stable Bi(012) was selected as the substrate. To model a realistic electrolyte microenvironment, explicit water molecules were added to stabilize Cl^- ions and simulate the local hydrogen bonding network while also considering computational efficiency, 10 H_2O molecules, 1 Cl atom, and 1 K atom (to balance charge) are added to the Bi(012) surface, denoted as Bi(012)@H_2O+Cl (Figure 5C). A control model, Bi(012)@H_2O, containing only 10 H_2O molecules without Cl and K atoms is constructed for comparison. Additionally, a bare Bi(012) model, without considering the electrolyte microenvironment, as used in the DFT optimization of metal active species in Figure 1, was also constructed to identify the possible effect of the H_2O molecule network. Bi(012)@H_2O and Bi(012) show ΔG_{RDS} values of 0.43 and 0.44 eV for the HCOOH formation/desorption step, respectively, indicating the negligible effect of the water molecule network on ΔG_{RDS}. When a Cl atom is added in the Bi(012)@H_2O+Cl model, the corresponding ΔG profile becomes thermodynamically spontaneous, demonstrating the boosting effect of surficial Cl^- ions on Bi(012) for $CO_2RR_{formate}$ (Figure 5D). Meanwhile, the surficial Cl^- ions can also suppress competing HER, as evidenced by the significantly increased ΔG of 0.40 eV for Bi(012)@H_2O+Cl compared to 0.045 eV for Bi(012)@H_2O and 0.047 eV for Bi(012) (Figure 5E). The enhanced CO_2RR and suppressed HER can be attributed to the downshift of the *p*-band center by surficial Cl^- ions, which weakens the adsorption of $^*OCHO$ and $^*H$ intermediates (Figure S21, Supporting Information).[29] Additionally, differential charge and population analyses support the decreased electron density of surficial Bi atoms due to Cl^- ions. The Bi site in Bi(012)@H_2O+Cl exhibits a more positive charge (+0.019) compared to Bi(012)@H_2O (+0.012), which is consistent with the higher binding energy of h-Bi@Cl compared to h-Bi in Bi 4*f* XPS spectra (Figure 5F). In addition to theoretical insights, the role of surficial Cl^- ions can also be understood from an experimental perspective, as reflected by a larger ECSA and lower R_{ct} of h-Bi@Cl compared to h-Bi, indicating more exposed active sites and faster interfacial charge transfer kinetics in the presence of Cl^- ions (Figure S22, Supporting Information). Notably, when the h-Bi electrode is immersed in $KHCO_3$ containing Cl^- ions, the maximum $FE_{formate}$ and $J_{formate}$ recover from 85.5 to 91.5% and from 43.8 to 50.8 $mA{\cdot}cm^{-2}$, respectively. These results underscore the pivotal role of interfacial Cl^- ions in enhancing CO_2RR while ruling out a substantial contribution from K^+ ions in the electrolyte. This enhancement is also observed in other halogen-containing electrolytes, such as Br^-, indicating the universal function of interfacial halogen ions in enhancing CO_2RR (Figure S23, Supporting Information).

3. Conclusion

To develop an efficient CO_2RR system for practical applications, we propose a strategy that synergistically engineers the electrochemical system to achieve industrial-level formate production. This is accomplished by replacing anodic OER with MOR and creating a reaction-favoring microenvironment through interfacial Cl^- ions for cathodic CO_2RR. The metal species in the electrodes were initially screened through theoretical optimization, followed by the synthesis of binder-free electrodes via facile electrodeposition. The resulting Bi—NiOOH full cell achieves a $FE_{formate}$ of over 90% at the industrial-level current densities exceeding 100 $mA{\cdot}cm^{-2}$ for both the cathode and anode, enabling concurrent industrial-level formate electrosynthesis. This study demonstrates the role of the local anion microenvironment in electrocatalysis and provides valuable insights into concurrent, industrial-level product synthesis.

4. Experimental Section

Synthesis: Both the anode and cathode were synthesized via electrodeposition in a three-electrode system, using an Ag/AgCl electrode (3 M KCl) and graphite rod as the reference and counter electrodes, respectively. For the anode, h-Ni$(OH)_2$ was deposited on Ni foam by electrodeposition in $Ni(NO_3)_3$ (50 mL, 0.1 M) at a voltage of −2.0 V for 15 min. For the cathode, the h-BiOCl precursor was deposited on CFP through a first-step electrodeposition in HCl (50 mL, 2.5 M) containing $Bi(NO_3)_3{\cdot}6H_2O$ (2 g) at −1.0 V for 90 s. The h-Bi@Cl was then obtained by transferring the precursor into $KHCO_3$ (50 mL, 0.1 M) for a second-step electroreduction at −1.5 V for 5 min. The control sample, h—Bi, was prepared by extending the second-step electroreduction time to 15 min, followed by thorough washing of the electrode multiple times to ensure complete removal of Cl^- ions.

Electrochemical Measurements: The MOR/OER tests were conducted in a three-electrode system, with a Hg/HgO electrode (1 M KOH) and a graphite rod as reference and counter electrodes, respectively. The working electrodes were first activated by CV at a scan rate of 50 $mV{\cdot}s^{-1}$ for 30 cycles. MOR and OER polarization curves were collected in a 50 mL Ar-saturated 1 M KOH solution containing methanol (1 M) and KOH (1 M), respectively, using LSV at a scan rate of 5 $mV{\cdot}s^{-1}$. Product analysis of MOR was performed by chronopotentiometry with current densities ranging from 50 to 300 $mA{\cdot}cm^{-2}$ for 1 h of electrocatalysis. Following the reaction, liquid products were analyzed by NMR spectroscopy (400 MHz, conventional). All measured potentials versus the Hg/HgO electrode were converted to RHE according to the equation of $E_{RHE} = E_{Hg/HgO} + 0.059 \times pH + 0.098$. All polarization curves were corrected by 95% iR_s compensation. The R_s was measured by electrochemical impedance spectroscopy (EIS) at 0 V versus Hg/HgO.

The CO_2RR experiments were performed in a customized H-type electrochemical cell with two compartments separated by a Nafion117 proton exchange membrane (three-electrode system) and a GDE flow cell separated by anion exchange membrane (two-electrode system). For the H-type cell, 0.5 M $KHCO_3$ was used as the electrolyte. The working electrode and Pt electrode were placed in separate compartments to avoid Pt contamination. An Ag/AgCl electrode (3 M KCl) and Pt foil were used as the reference

and counter electrodes, respectively. All potentials were converted to RHE using $E_{RHE} = E_{Ag/AgCl} + 0.059 \times pH + 0.209$. For the GDE flow cell, 1 M KOH was used as the electrolyte, and nickel foam was used as the counter electrode. The CO_2 flow rate of 30 mL min^{-1} was regulated using a mass flow controller and verified with another identical mass flow meter at the outlet. For H-type cell experiments, the catholyte was first purged with CO_2 for 20 min, followed by 20 consecutive CV scans from 0 to −0.4 V to activate the catalyst and desorb residual gases. In flow cell measurements, this pretreatment step was omitted. The reduction time was set to 30 min using chronoamperometry in the H-type cell (potential range: from −0.7 to −1.4 V) and chronopotentiometry in the GDE flow cell (current density rage: 50–300 mA·cm^{-2}). Gas products were quantitatively detected by online GC, and liquid products were analyzed by NMR spectroscopy (400 MHz, water suppression). The full-cell experiments were conducted in a similar way to the CO_2RR experiments in the GDE flow cell, with the anodic electrolyte replaced by 1 M KOH containing methanol (1 M).

In Situ Electrospectroscopy: In situ Raman spectroscopy was performed within the same potential windows as those applied for MOR and CO_2RR using a custom-designed electrochemical cell. For MOR, the cell was filled with 1 M KOH containing 1 M methanol, utilizing a Hg/HgO reference electrode (1 M KOH) and a Pt wire counter electrode. For CO_2RR, the cell contained CO_2-saturated 0.5 M $KHCO_3$, with an Ag/AgCl reference electrode (3 M KCl) and a Pt wire counter electrode. Measurements employed a 785 nm excitation laser (5 mW power) and a 50× long-distance objective lens, with Raman shifts calibrated against a Si wafer (520 cm^{-1}). Each spectrum was collected over a 10-s period with three accumulations. In situ FTIR spectroscopy, specifically electrochemical attenuated total reflection-surface enhanced infrared absorption spectroscopy (ATR-SEIRAS), was conducted using a Thermo Fisher Scientific Nicolet iS50 equipped with a liquid N_2-cooled mercury cadmium telluride (MCT) detector. The electrochemical workstation was a CS350A model (Corrtest). A gold-coated single-crystal Si substrate, with the gold layer applied to enhance spectroscopic signals, served as the working electrode. The catalyst was ultrasonicated in ethanol to form a dispersion and subsequently drop-cast onto the gold-coated Si substrate for analysis.

Theoretical Calculations: Free energy profile calculations were performed using the DMol^3 package with DFT.[30] The generalized gradient approximation (GGA) with the Perdew–Burke–Ernzerhof (PBE) functional was used to describe electronic exchange and correlation effects.[31] The core treatment was based on density functional semicore pseudopotential (DSPP), which included a certain degree of relativistic correction. A dispersion-corrected DFT (DFT-D) scheme was used to describe van der Waals (vdW) interactions. The solution effect of water was accounted for using a conductor-like screening model (COSMO).[32] During coordinate relaxation, the tolerances for energy and force were 1×10^{-5} Ha and 0.002 Ha $Å^{-1}$, respectively, with a maximum displacement of 5×10^{-3} Å. The K points meshing for the Brillouin zone was set at 4 × 4 × 1, and the global orbital cutoff was set at 5.0 Å after a convergence test.

Differential charge density, population analysis, and density of state were carried out using the Cambridge Serial Total Energy Package (CASTEP). Ultrasoft pseudopotentials were generated on the fly. The cutoff energy for the plane wave basis set was 489 eV, and the Monkhorst–Pack k-point mesh was sampled with a separation of ≈0.04 $Å^{-1}$ in the Brillouin zone.

Materials Characterizations: The morphologies and structures of the as-prepared catalysts were examined using scanning electron microscopy (SEM, Tescan VEGA3), high-resolution transmission electron microscopy (HRTEM, JEOL, JEM-F200), X-ray diffraction (XRD, Rigaku SmartLab 9kW-Advance), and Raman spectroscopy (Horiba Ltd., LabRAM Aramis). X-ray photoelectron spectroscopy (XPS, ThermoFischer, ESCALAB Xi+, Al *Kα*) was used to analyze surface chemical states and element contents.

Supporting Information

Supporting Information is available from the Wiley Online Library or from the author.

Acknowledgements

This work was jointly supported by the University Grant Council of Hong Kong (PolyU15217521), the Hong Kong Polytechnic University (Q-CDAG), the National Research Foundation of Korea (NRF-2022H1D3A2A01096400) of the Korean Government (MSIT), the National Key Research and Development Program of China (2021YFA1500900), the Natural Science Foundation of Jiangsu Province, Major Project (BK20212005), and the National Natural Science Foundation of China (52071174).

Conflict of Interest

The authors declare no conflict of interest.

Data Availability Statement

The data that support the findings of this study are available from the corresponding author upon reasonable request.

Keywords

CO_2 reduction reaction, formate, interfacial Cl^- ion, local microenvironment, methanol oxidation reaction

Received: February 25, 2025
Revised: March 31, 2025
Published online: April 16, 2025

[1] a) M. McNutt, *Science* **2019**, *365*, 411; b) G. Wen, B. Ren, X. Wang, D. Luo, H. Dou, Y. Zheng, R. Gao, J. Gostick, A. Yu, Z. Chen, *Nat. Energy* **2022**, *7*, 978.
[2] a) E. S. Sanz-Perez, C. R. Murdock, S. A. Didas, C. W. Jones, *Chem. Rev.* **2016**, *116*, 11840 b) Y. Chen, J. Zhang, L. Yang, X. Wang, Q. Wu, Z. Hu, *Electrochem. Energy Rev.* **2022**, *5*, 11.
[3] a) Y. Chen, J. Zhang, J. Tian, Y. Guo, F. Xu, Y. Zhang, X. Wang, L. Yang, Q. Wu, Z. Hu, *Adv. Funct. Mater.* **2023**, *33*, 2214658; b) Y. Chen, M. Xia, C. Zhou, Y. Zhang, C. Zhou, F. Xu, B. Feng, X. Wang, L. Yang, Z. Hu, Q. Wu, *ACS Nano* **2023**, *17*, 22095; c) X. Fan, C. Liu, X. He, Z. Li, L. Yue, W. Zhao, J. Li, Y. Wang, T. Li, Y. Luo, D. Zheng, S. Sun, Q. Liu, L. Li, W. Chu, F. Gong, B. Tang, Y. Yao, X. Sun, *Adv. Mater.* **2024**, *36*, 2401221; d) Z. Zhang, D. Li, Y. Tu, J. Deng, H. Bi, Y. Yao, Y. Wang, T. Li, Y. Luo, S. Sun, D. Zheng, S. A. C. Carabineiro, Z. Chen, J. Zhu, X. Sun, *SusMat* **2024**, *4*, 193.
[4] a) J. Zhang, Y. Chen, F. Xu, Y. Zhang, J. Tian, Y. Guo, G. Chen, X. Wang, L. Yang, Q. Wu, Z. Hu, *Small* **2023**, *19*, 2301577; b) G. Li, C. Zhang, Y. Liu, Y. Song, W. Guo, L. Huang, J. Su, Q. Zhang, Y. Xin, T. Feng, X. Cao, M. He, T. K. Kwok, J. W. Y. Lam, Z. Jin, B. Z. Tang, Z. Wang, R. Ye, *Adv. Mater.* **2024**, 2409390.
[5] H. Shen, H. Jin, H. Li, H. Wang, J. Duan, Y. Jiao, S. Z. Qiao, *Nat. Commun.* **2023**, *14*, 2843.
[6] J. Bi, P. Li, J. Liu, Y. Wang, X. Song, X. Kang, X. Sun, Q. Zhu, B. Han, *Angew. Chem., Int. Ed.* **2023**, *62*, 202307612.
[7] a) G. Jia, Y. Wang, M. Sun, H. Zhang, L. Li, Y. Shi, L. Zhang, X. Cui, T. W. B. Lo, B. Huang, J. C. Yu, *J. Am. Chem. Soc.* **2023**, *145*, 14133 b) S. Yang, M. Jiang, W. Zhang, Y. Hu, J. Liang, Y. Wang, Z. Tie, Z. Jin, *Adv. Funct. Mater.* **2023**, *33*, 2301984.
[8] a) B. Zhang, Y. Wu, P. Zhai, C. Wang, L. Sun, J. Hou, *Chin. J. Catal.* **2022**, *43*, 3062 b) Y. Guan, M. Liu, X. Rao, Y. Liu, J. Zhang, *J. Mater. Chem. A* **2021**, *9*, 13770.

[9] a) Z. Huang, R. G. Grim, J. A. Schaidle, L. Tao, *Energy Environ. Sci.* **2021**, *14*, 3664 b) M. G. Kibria, J. P. Edwards, C. M. Gabardo, C. T. Dinh, A. Seifitokaldani, D. Sinton, E. H. Sargent, *Adv. Mater.* **2019**, *31*, 1807166.
[10] a) M. Jiang, H. Wang, M. Zhu, X. Luo, Y. He, M. Wang, C. Wu, L. Zhang, X. Li, X. Liao, Z. Jiang, Z. Jin, *Chem. Soc. Rev.* **2024**, *53*, 5149 b) J. Chen, X. Peng, Z. Li, B. Yang, Q. Zhang, J. Lu, L. Lei, Y. Hou, *Adv. Mater.* **2024**, 2409106.
[11] a) E. W. Lees, B. A. W. Mowbray, F. G. L. Parlane, C. P. Berlinguette, *Nat. Rev. Mater.* **2021**, *7*, 55 b) C. P. O'Brien, R. K. Miao, A. Shayesteh Zeraati, G. Lee, E. H. Sargent, D. Sinton, *Chem. Rev.* **2024**, *124*, 3648.
[12] a) S. Iqbal, B. Safdar, I. Hussain, K. Zhang, C. Chatzichristodoulou, *Adv. Energy Mater.* **2023**, *13*, 2203913; b) C. Rong, K. Dastafkan, Y. Wang, C. Zhao, *Adv. Mater.* **2023**, *35*, 2211884.
[13] a) S. Verma, S. Lu, P. J. A. Kenis, *Nat. Energy* **2019**, *4*, 466 b) S.-Q. Liu, M.-R. Gao, S. Wu, R. Feng, Y. Wang, L. Cui, Y. Guo, X.-Z. Fu, J.-L. Luo, *Energy Environ. Sci.* **2023**, *16*, 5305.
[14] X. Liu, Y. Wang, Z. Dai, D. Gao, X. Zhao, *J. Energy Chem.* **2024**, *92*, 705.
[15] Q. Fang, S. Ye, L. Zheng, H. Wang, L. Hu, W. Gu, L. Wang, L. Shi, C. Zhu, *ACS Catal.* **2024**, *14*, 9235.
[16] A. Xu, T. Liu, D. Liu, W. Li, H. Huang, S. Wang, L. Xu, X. Liu, S. Jiang, Y. Chen, M. Sun, Q. Luo, T. Ding, T. Yao, *Angew. Chem., Int. Ed.* **2024**, *63*, 202410545.
[17] a) H. Cheng, B. Dong, Q. Liu, F. Wang, *J. Am. Chem. Soc.* **2023**, *145*, 26858 b) Y. Yan, J. Zhong, R. Wang, S. Yan, Z. Zou, *J. Am. Chem. Soc.* **2024**, *146*, 4814.
[18] a) X. Sun, R. B. Araujo, E. C. Dos Santos, Y. Sang, H. Liu, X. Yu, *Chem. Soc. Rev.* **2024**, *53*, 7392 b) H. Xu, D. Cheng, D. Cao, X. C. Zeng, *Nat. Catal.* **2024**, *7*, 207
[19] a) Y. Zhang, B. Feng, M. Yan, Z. Shen, Y. Chen, J. Tian, F. Xu, G. Chen, X. Wang, L. Yang, Q. Wu, Z. Hu, *Nano Res.* **2023**, *17*, 3769 b) Y. Hao, D. Yu, S. Zhu, C.-H. Kuo, Y.-M. Chang, L. Wang, H.-Y. Chen, M. Shao, S. Peng, *Energy Environ. Sci.* **2023**, *16*, 1100.
[20] a) Z. Li, M. Liu, J. Yan, L. Y. S. Lee, *Chem. Eng. J.* **2023**, *473*, 145293; b) B. Zhu, B. Dong, F. Wang, Q. Yang, Y. He, C. Zhang, P. Jin, L. Feng, *Nat. Commun.* **2023**, *14*, 1686.
[21] a) X. Feng, H. Zou, R. Zheng, W. Wei, R. Wang, W. Zou, G. Lim, J. Hong, L. Duan, H. Chen, *Nano Lett.* **2022**, *22*, 1656 b) C. Li, Z. Liu, X. Zhou, L. Zhang, Z. Fu, Y. Wu, X. Lv, G. Zheng, H. Chen, *Energy Environ. Sci.* **2023**, *16*, 3885.
[22] T. Wang, J. Chen, X. Ren, J. Zhang, J. Ding, Y. Liu, K. H. Lim, J. Wang, X. Li, H. Yang, Y. Huang, S. Kawi, B. Liu, *Angew. Chem., Int. Ed.* **2023**, *62*, 202211174.
[23] Z.-Z. Niu, L.-P. Chi, R. Liu, Z. Chen, M.-R. Gao, *Energy Environ. Sci.* **2021**, *14*, 4169.
[24] a) G. Li, G. Han, L. Wang, X. Cui, N. K. Moehring, P. R. Kidambi, D. E. Jiang, Y. Sun, *Nat. Commun.* **2023**, *14*, 525; b) Y. Qin, W. Zhang, F. Wang, J. Li, J. Ye, X. Sheng, C. Li, X. Liang, P. Liu, X. Wang, X. Zheng, Y. Ren, C. Xu, Z. Zhang, *Angew. Chem., Int. Ed.* **2022**, *61*, 202200899.
[25] a) C. Chen, Y. Li, P. Yang, *Joule* **2021**, *5*, 737 b) X. Lu, C. Zhu, Z. Wu, J. Xuan, J. S. Francisco, H. Wang, *J. Am. Chem. Soc.* **2020**, *142*, 15438.
[26] P. A. Christensen, D. Linares-Moya, *J. Phys. Chem. C* **2009**, *114*, 1094.
[27] a) H. Qin, Y. Ye, G. Lin, J. Zhang, W. Jia, W. Xia, L. Jiao, *ACS Catal.* **2024**, *14*, 16234 b) Y. Qi, Y. Zhang, L. Yang, Y. Zhao, Y. Zhu, H. Jiang, C. Li, *Nat. Commun.* **2022**, *13*, 4602.
[28] X. Yu, Y. Xu, L. Li, M. Zhang, W. Qin, F. Che, M. Zhong, *Nat. Commun.* **2024**, *15*, 1711.
[29] X. Yue, L. Cheng, F. Li, J. Fan, Q. Xiang, *Angew. Chem., Int. Ed.* **2022**, *61*, 202208414.
[30] a) B. Delley, *J. Chem. Phys.* **1990**, *92*, 508 b) B. Delley, *J. Chem. Phys.* **2000**, *113*, 7756.
[31] J. P. Perdew, K. Burke, M. Ernzerhof, *Phys. Rev. Lett.* **1996**, *77*, 3865.
[32] A. Klamt, G. Schüürmann, *J. Chem. Soc., Perkin Trans. 2* **1993**, 799.